



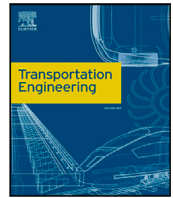
Simulation-based assessment of wheel torque allocation strategies on heavy vehicles with drivetrains on multiple axles

Downloaded from: <https://research.chalmers.se>, 2025-04-20 06:37 UTC

Citation for the original published paper (version of record):

Janardhanan, S., Henderson, L., Jonasson, M. et al (2025). Simulation-based assessment of wheel torque allocation strategies on heavy vehicles with drivetrains on multiple axles. *Transportation Engineering*, 20. <http://dx.doi.org/10.1016/j.treng.2025.100322>

N.B. When citing this work, cite the original published paper.



Full length article

Simulation-based assessment of wheel torque allocation strategies on heavy vehicles with drivetrains on multiple axles

Sachin Janardhanan^{a,b,*}, Leon Henderson^b, Mats Jonasson^a, Bengt Jacobson^a, Esteban R. Gelso^b

^a Chalmers University of Technology, M building, Hörsalsvägen 7 A, 412 96, Göteborg, Sweden

^b Volvo Group Trucks Technology, Gropegårdsgatan 10, 417 15, Göteborg, Sweden

ARTICLE INFO

Keywords:

Battery electric vehicles
Power losses
Drivetrain
Actuator coordination

ABSTRACT

Battery electric heavy vehicles with a drivetrain on each axle and friction brake on each wheel offer significant opportunities to enhance vehicle performance and energy efficiency. This paper presents three actuator coordination algorithms for an all-wheel driven heavy vehicle to influence the wheel torque with the aim of optimising the power efficiency and vehicle stability. Two of these algorithms exploit the principle of instantaneous power loss minimisation by using the power loss models of actuators. The wheel force limits were included as a constraint to ensure safe vehicle operation. These strategies were simulated using a high-fidelity vehicle model, including simplified models for the powertrain and friction brakes. Measures such as the power loss of the actuators, longitudinal tyre slip losses, and energy consumption of the coordination strategies during a realistic drive cycle were analysed. Results show that the power loss minimisation algorithm including idle losses in the decision logic, can reduce the energy consumption by up to 7% compared to a strategy only maximising tyre grip.

1. Introduction

The adoption of battery-electric heavy vehicles (BEVs) for long-haul transport is currently limited by factors such as range anxiety, inconsistent vehicle performance, and high operational costs. For typical European 4X2 tractor semi-trailers with internal combustion engines (ICEs), fuel consumption during long-haul cycles is around 30 L/100 km [1]. These vehicles have variable fuel tank capacities (300–600 litres), low diesel fuel costs, and a dense refuelling infrastructure, making driving range a less critical performance metric. In contrast, BEVs, which lack a similar charging infrastructure and having a finite driving range influenced by battery capacity, face greater challenges [2,3].

The primary challenge to the widespread adoption of BEVs for long-haul cycles is the driving range, which is influenced by multiple factors, including vehicle design parameters such as aerodynamic drag, rolling resistance, battery capacity, and gross combination weight (GCW). Environmental factors like weather, traffic conditions, and infrastructure also impact performance [4,5]. While vehicle design can be limited by legislation and infrastructure constraints, driving style, charging strategy, and the control of vehicle actuators offer potential for improving performance [6].

To address these challenges, this study focuses on developing energy-efficient wheel torque allocation strategies that minimise power losses

while ensuring safe vehicle operation. These strategies consider not only the power losses from electric drivetrains but also idle losses, tyre-road friction limits, and actuator operating limits. By integrating these factors into actuator coordination for BEVs, this study aims to optimise energy efficiency in real-world long-haul driving conditions [7,8].

1.1. Background

BEVs have the potential to revolutionise long-haul transport, but their adoption is constrained by performance limitations, particularly driving range. BEVs require effective coordination between various motion actuators, such as electric drivetrains, friction brakes, suspension systems, and steering, to optimise performance. The optimisation of energy consumption and the reduction of power losses are critical factors for increasing the range and operational efficiency of BEVs.

Vehicle motion control (VMC) algorithms are key to achieving optimal coordination of these actuators. By integrating and coordinating motion actuators, VMC algorithms generate the desired wheel torques and satisfy primary and secondary objectives such as minimising energy consumption, actuator wear, and power usage [8]. For BEVs, representing an over-actuated system, control allocation (CA)

* Corresponding author at: Chalmers University of Technology, M building, Hörsalsvägen 7 A, 412 96, Göteborg, Sweden.

E-mail addresses: sachin.janardhanan@volvo.com (S. Janardhanan), leon.henderson@volvo.com (L. Henderson), mats.jonasson@chalmers.se (M. Jonasson), bengt.jacobson@chalmers.se (B. Jacobson), esteban.gelso@volvo.com (E.R. Gelso).

<https://doi.org/10.1016/j.treng.2025.100322>

Received 10 October 2024; Received in revised form 12 March 2025; Accepted 13 March 2025

Available online 25 March 2025

2666-691X/© 2025 The Authors. Published by Elsevier Ltd. This is an open access article under the CC BY license (<http://creativecommons.org/licenses/by/4.0/>).

Symbol	Description	unit
$a_{x,req}$	Longitudinal acceleration request	m/s^2
$v_{x,req}$	Longitudinal velocity request	m/s
ϕ_{ry}	Road grade	rad
$F_{x,res}$	Total longitudinal resistive force	N
$v_{x,act}$	Actual longitudinal vehicle speed	m/s
$F_{x,ff}$	Feed-forward controller force request	N
$F_{x,fb}$	Feedback longitudinal force request	N
$F_{x,drv}$	Longitudinal force request from the driver model	N
δ_{req}	Steering angle requests at the wheel	rad
$F_{x,req}$	Regulated longitudinal force request	N
$F_{xminEM,i}$	Minimum or negative force limit of electric drivetrain on an axle	N
$F_{xmaxEM,i}$	Maximum or positive force limit of electric drivetrain on an axle	N
$F_{xreqEM,i}$	Force request to the electric drivetrain from the actuator coordinator	N
$F_{xEM,i}$	Force corresponding to generated actual torque by the electric drivetrain	N
$T_{reqEM,i}$	Torque request to the electric drivetrain from the actuator coordinator	Nm
$T_{EM,i}$	Actual torque request to the wheel from the electric drivetrain	Nm
$F_{xminbrk,i}$	Minimum or negative force limit of the friction brakes on an axle	N
$F_{xmaxbrk,i}$	Maximum or positive force limit of the friction brakes on an axle	N
$F_{xreqbrk,i}$	Force request to the friction brakes from the actuator coordinator	N
$T_{reqbrk,i}$	Torque request to the friction brakes from the actuator coordinator	Nm
$T_{brk,i}$	Actual torque request to the wheel from the friction brakes	Nm
$F_{z,i}$	Actual normal load on an axle	N
$F_{y,i}$	Estimated lateral force generated on an axle	N
$F_{xlim,i}$	Longitudinal wheel force limit of an axle	N
$F_{xreq,i}$	Longitudinal wheel force request to an axle	N
$P_{Batt,cons}$	Total electrical power consumed from the battery	kW
$P_{Batt,gen}$	Total electrical power regenerated to the battery	kW
$P_{EM,i}$	Instantaneous mechanical power generated by the electric drivetrain	kW
$P_{lossEM,i}$	Instantaneous power loss of the electric drivetrain	kW
$P_{lossbrk,i}$	Instantaneous power loss of the friction brakes	kW
$P_{loss,sx}$	Total Longitudinal tyre slip loss	kW
$P_{loss,rr}$	Total rolling resistance loss	kW
$P_{mechEM,i}$	Mechanical power of an electric machine	kW
$P_{elEM,i}$	Electric power associated with an electric machine	kW
$F_{xw,i}$	Longitudinal force on a wheel	N
$v_{xw,i}$	Longitudinal speed of a wheel	m/s
$\omega_{w,i}$	Rotational speed of a wheel	rad/s
$r_{ew,i}$	Effective rolling radius of a wheel	m
$F_{zw,i}$	Normal load on a wheel	N
$T_{brkw,i}$	Braking torque on a wheel	Nm
$v_{xact,i}$	Longitudinal speed of an axle measured at the centre	m/s

techniques play a pivotal role in coordinating actuator outputs while meeting the vehicle's motion requirement [9].

The complexity of optimising BEV actuator coordination increases with the inclusion of multiple actuators, such as dual-motor systems or systems with multiple axles. Additionally, power losses from various components, including electric machines, inverters, and tyres, must be considered in the optimisation process. These losses, when accurately modelled, can lead to more effective torque allocation strategies that improve energy efficiency and overall performance.

1.2. Literature review

Many studies have focused on CA-based wheel torque distribution strategies for enhancing vehicle handling, safety, and energy efficiency [9–21]. These strategies often use optimisation algorithms and real-time control to minimise power losses and improve handling. For instance, previous studies in [10,11,13,21] explore torque vectoring for multi-motor electric vehicles to improve understeer characteristics. In contrast, other studies, such as [9,14,16–20], focus on longitudinal dynamics, optimising algorithms to maximise energy efficiency while maintaining vehicle stability. However, these studies often rely on ideal conditions such as constant road friction, precise torque measurements, and infinite computational resources. Such assumptions can lead to discrepancies between simulated and real-world performance. Furthermore, many studies focus on passenger vehicles or limited driving cycles, which makes it difficult to apply their findings to heavy vehicles operating in complex, real-world conditions.

Another difference observed in the literature is the sources of power losses included in wheel torque allocation algorithms. For instance, in [10–12], electric machine, transmission, and tyre losses, obtained from experiments, are analysed, while other studies, such as [9,13,20], focus primarily on electric machine and inverter losses. Tyre-related power losses were modelled with improved accuracy in [20] compared to [9,13]. However, tyre slip models often oversimplify tyre-road interactions, potentially underestimating energy losses in dynamic conditions. Additionally, inclusion of friction brake losses in the optimisation formulations are limited in literature.

Furthermore, with the different approximations of losses, optimisation methods also differ including both offline and online schemes [9,12,13,15,16]. Studies, such as [9,12,13], especially provide insights into offline optimisation strategies. Offline optimisation is typically more computationally intensive and requires pre-calculation of torque allocation strategies for various driving conditions. In contrast, online optimisation adjusts the torque distribution in real-time, making it more suitable for dynamic driving conditions. The literature also suggests that higher-order polynomial models or advanced optimisation techniques, such as machine learning approaches, may be necessary to accurately represent system behaviour in high or low load conditions [9,15]. For example, in [16], a method that satisfies the KKT conditions was presented for a 6X6 heavy vehicle, especially to handle the non-convex power loss characteristics. The KKT-based approach helps address the challenges of optimising the torque distribution for non-convex problems, but its application is computationally demanding and may not be suitable for real-time systems without significant simplifications or approximations.

Previous studies have also examined idle losses and torque distribution strategies under different drivetrain configurations, including dual-motor and multi-axle vehicles [16–19,22,23]. In [18], different algorithms to optimise clutch usage for wear and comfort are presented. In [23], the authors proposed a system-level optimisation of power losses in an electric vehicle (EV) driven by front and rear induction motors under steady state conditions, avoiding mechanical clutches. However, many of these studies focus on passenger vehicles, limited test manoeuvres involving complex operation of mechanical clutches, making it difficult to apply their findings to heavy vehicle applications.

1.3. Contributions

This study complements the literature through the following contributions:

- Introducing a novel actuator coordination strategy for power loss minimisation with the inclusion of idle losses (power loss when zero output torque) and wheel force limits to ensure safe vehicle operation, which can be extended to cases with multiple axles and actuators.
- Comparing alternative actuator coordination strategies using a high-fidelity heavy vehicle model, comprehensive power loss models, and realistic transport operation.
- Proposing a method for evaluating and analysing the actuator coordination for 2-axle heavy vehicles with different electric drivetrains on the front and rear axles.

1.4. Layout

The remainder of this paper is organised as follows. Section 2 introduces the problem formulation solved via optimisation. Section 3 describes the different power loss models used in the objective function of the optimisation and for the analysis of the results. Section 4 specifies the vehicle configuration and driving cycle. Section 5 presents the models used for the driver, control system, actuators, and vehicle, including the interfaces. In Section 6 different wheel torque allocation strategies are described. Section 7 presents the results, discussion, and conclusions of the analysis in Section 8.

In this paper, the symbols representing the variables and parameters concerning the axle and wheels are described using the following subscripts: i , axle; w , wheel; EM , electric machine; and brk , friction brake. The symbols are specified using the following format $entity_{actuator,axle}$, or as $entity_{axle}$, for e.g. $F_{xw,i}$, $F_{z,i}$. The axles are numbered starting from the front axle of the tractor as 1, followed by the rear axle as 2, and in that sequence until the last axle of the trailer as 5.

2. Problem formulation

In this paper, wheel torque allocation is described as a CA problem solved by optimising actuator requests \mathbf{u}^* . The optimisation variables chosen here are expressed as forces rather than torques, which are then rescaled to torques after optimisation. The optimal actuator coordination problem is solved for \mathbf{u} , a vector of actuator requests. The objective function $\Phi(\mathbf{u}, \mathbf{x})$ is expressed as a function that minimises power losses, where \mathbf{x} is a vector of non-optimised variables like state variables.

$$\mathbf{u}^* = \arg \min_{\mathbf{u}} (\Phi(\mathbf{u}, \mathbf{x})) \quad (1)$$

$$\text{s.t } \mathbf{v} = f(\mathbf{x}, \mathbf{u})$$

$$\mathbf{u} \leq h(\mathbf{x}, \mathbf{u})$$

$$\mathbf{u}_{lb}(\mathbf{x}, \mathbf{u}) \leq \mathbf{u} \leq \mathbf{u}_{ub}(\mathbf{x}, \mathbf{u})$$

A nonlinear mapping exists between the requested global forces \mathbf{v} on the vehicle and actuator forces at each instant.

$$\mathbf{v} = f(\mathbf{x}, \mathbf{u}(t)) \quad (2)$$

Additionally, a nonlinear mapping exists between the tyre forces at the contact patch and the applied actuator forces, with a feasible region associated with them.

$$\mathbf{u} \leq h(\mathbf{x}, \mathbf{u}(t)) \quad (3)$$

By solving the actuator coordination problem at every instant, a linear mapping is satisfactorily performed for the nonlinear system, which allows (2) and (3) to be expressed with the actuator constraints as follows:

$$\mathbf{v} = B \cdot \mathbf{u}(t) \quad (4)$$

$$\mathbf{u} \leq G \cdot \mathbf{u}(t) \quad (5)$$

where B denotes the control effectiveness matrix, and G denotes the axle capability matrix.

Similarly, the actuator upper and lower bounds \mathbf{u}_{lb} and \mathbf{u}_{ub} respectively, representing the positive and negative force limits, can be rewritten as:

$$\mathbf{u}_{lb}(\mathbf{x}, \mathbf{u}(t)) \leq \mathbf{u}(t) \leq \mathbf{u}_{ub}(\mathbf{x}, \mathbf{u}(t)) \quad (6)$$

3. Sources of power losses

Vehicle motion is associated with power dissipation from numerous sources, such as aerodynamic losses, rolling resistance losses, tyre slip losses, electric powertrains, cooling systems, batteries, and auxiliary systems [24]. This requires a detailed understanding of the characteristics and physics of power loss sources. Here, the important sources of power losses influenced by wheel torque allocation are used to compare the different strategies. Aerodynamic losses proportional to the third power of the vehicle speed were excluded from the analysis. This reason is that the vehicle speed remained nearly constant in the coordination strategies.

3.1. Tyre slip losses

For pneumatic tyres, when a driving or braking torque is applied to a wheel, force is generated at the tyre-road contact patch. The generated longitudinal force is due to the relative motion between the road surface and rubber tread of the tyre, which can be expressed by a term called longitudinal slip. This longitudinal slip phenomenon can be expressed as a relative slip velocity and is defined as the difference between the translational velocity of the wheel centre and rotational velocity of the wheel multiplied by the effective wheel radius. Thus, the slip power loss [25] for the whole vehicle, assuming that the torque is distributed equally between two wheels on an axle, can be expressed as follows:

$$P_{loss,sx} = \sum_i 2 \cdot F_{xw,i} (v_{xw,i} - \omega_{w,i} \cdot r_{ew,i}) \quad (7)$$

where $F_{xw,i}$ is the longitudinal force generated at the tyre-road contact patch of a single wheel, $r_{ew,i}$ is the effective rolling radius of the tyre, $v_{xw,i}$ is the longitudinal velocity of the wheel centre and $\omega_{w,i}$ is the rotational velocity of the tyre. In this study, the tyre slip losses, namely longitudinal slip, were only analysed due to the wheel torque coordination and are not minimised.

The analysis of lateral tyre slip losses is excluded in this study because the lateral acceleration levels generated during the driving cycle are predominantly below $\pm 0.4 \text{ m/s}^2$, representing near straight line driving conditions. Additionally, due to the high friction levels considered between the tyre-road contact, the wheel forces produced are well within the tyre force limits. Hence, the produced lateral slips did not influence the wheel torque allocation and they were nearly same for the strategies described in Section 6. Thus, their effects are considered small for the given application.

3.2. Rolling resistance losses

Another source of power dissipation due to the tyre characteristics during rolling, owing to the viscoelastic properties of the rubber compounds, is referred to as rolling resistance. Physically, this is due to the deformation of the rubber elements that contact the road surface and their return to the initial condition after a certain time, referred to as the hysteresis phenomenon [26]. As a result, some of the energy utilised in deforming the tyre is lost in the form of heat. The hysteresis phenomenon is caused by internal damping within the tyre, which leads to an offset in the pressure distribution in the rolling direction, which creates a resistive wheel moment. A number of factors for e.g., tyre

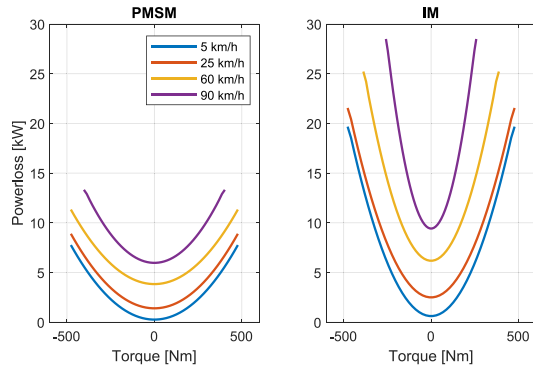


Fig. 1. Powerlosses of PMSM and IM expressed as function of the torque for different vehicle speeds. The loss at zero torque is called “idle loss”.

construction, operating speed, normal load, tyre pressure, ambient temperature, and applied torque. The rolling resistance moment can be expressed in simplified form can be expressed as

$$P_{loss,rr} = \sum_i 2 \cdot C_{rr} \cdot F_{z,wi} \cdot v_{x,wi} \quad (8)$$

where $F_{z,wi}$ is the vertical load on the wheel, $v_{x,wi}$ is the longitudinal velocity of the wheel centre and a constant $C_{r,r}$ is a constant called the rolling resistance coefficient. In this study, the rolling resistance coefficient was assumed to be the same for all wheels. The rolling resistance losses are only calculated and is not used as an objective to be minimised in the optimisation of wheel torque coordination.

3.3. Electric drivetrain losses

A Study in [27] indicated that the most prevalent types of electric machines used in BEVs are Induction machines (IM) and Permanent Magnet Synchronous Machines (PMSMs), which have different characteristics. This is primarily due to the design and construction of the machines along with the principle of operation. The losses in the machines can be broadly classified as copper, iron, windage, and friction losses. In this study, the losses were obtained from an electric drivetrain model [28] and were found to have a quadratic nature with torque, as shown in Fig. 1. It is important to utilise such a physical model as against using efficiency-derived power losses to capture the influence of idle losses in the control of electric drivetrains. This is because the efficiency-derived power loss model lacks information about zero torque and requires careful treatment.

Depending on the type of electric machine, switching off the power supply may not be sufficient to isolate the idle losses [22]. In permanent magnet synchronous machines, iron losses occur due to the rotation of the magnets even when the stator is not supplied with a three-phase electrical current. One solution to this problem consists of introducing a clutch between the PMSMs and the wheel so that the rotor remains stationary. However, this choice adds additional components to the vehicle, thereby affecting its weight and cost. Frequent engagement and disengagement also add to the wear and reduced life of the components. Another possibility is to use induction machines, which have the advantages of high reliability, robustness, and low cost. Exploiting the self-starting principle of the induction machines by requesting zero torque or switching off the associated inverter is sufficient to reduce the idle losses [22,23,28] but not completely. This eliminates the need of clutches in PMSMs. However, some losses, namely, windage and friction losses, would be added due to the rotation of the rotor with the wheel.

In BEVs with an electric drivetrain on each axle, the transmission transfers the torque and power from the machine to each wheel. The transmission parameters, namely the gear ratio, are specified

depending on the vehicle application and performance requirements. The transmission ratio also determines the operating point of the electric machine. Generally, the main contributors to transmission losses are speed, load, and temperature, leading to typical efficiencies within the range of 95%–97%. These losses can be divided into load-independent losses, such as spring losses and air windage, and load-dependent rolling and sliding. For load-dependent losses, physical equations can be used to model such losses. However, in this study, the load-dependent losses are simplified and expressed in terms of efficiency. The efficiency of a single gear ratio-based transmission on each axle i is simplified as $\eta_{trmn,i}$ and is assumed as a function of the gear ratio.

$$\eta_{trmn,i} = 0.99 \frac{gr_i}{3} \quad \text{where } i = 1, 2 \quad (9)$$

3.4. Electrical power conversion losses

In motoring mode, the electric drivetrain converts the electric power to mechanical power, and in generator mode mechanical to electrical. This conversion leads to inverter and battery losses. Battery losses are due to internal resistance, which converts chemical energy into heat energy instead of useful energy. Inverter losses, during AC-DC conversion are due to frequent switching at high voltages and are also converted to heat. These two losses are combined and modelled as the lumped conversion efficiency:

$$P_{mechEM,i} = P_{elEM,i} \cdot \eta_{mot,i} \quad (10)$$

$$P_{elEM,i} = P_{mechEM,i} \cdot \eta_{gen,i} \quad (11)$$

where as motoring $P_{mechEM,i}$ is the mechanical power, $P_{elEM,i}$ is the electrical power, $\eta_{mot,i}$ the motoring conversion efficiency and $\eta_{gen,i}$ is the regeneration conversion efficiency.

3.5. Friction brake losses

The actuation medium in the brake system of a heavy commercial vehicle is compressed air. The air is produced using a compressor and stored in air tanks. The air is then relayed to the brake actuators using the friction brake mechanism through tubes. The entire generation, storage, and transmission processes produces losses. These losses were neglected in this study because they remain constant and require detailed modelling of the pneumatic circuit.

In addition, to the above-mentioned loss, the friction brake mechanism converts the kinetic energy of the vehicle motion to heat energy. This is achieved when the rotating disc connected to the wheel contacts with non-moving friction pads connected to the chassis.

The heat losses due to friction braking can be expressed as a linear relation between the braking torque $T_{brkw,i}$ on a wheel and the rotational wheel speed $\omega_{w,i}$:

$$P_{loss,brk} = \sum_i 2 \cdot T_{brkw,i} \cdot \omega_{w,i} \quad (12)$$

4. Description of vehicle and its application

This section introduces the methodology, assumptions, and practical applications of wheel torque coordination strategies (see Fig. 2).

4.1. Vehicle and drivetrain configuration

The vehicle used to evaluate the wheel torque coordination strategies was a 4 × 4 tractor with a 3-axle semi-trailer as shown in Fig. 2. A distributed drivetrain topology on a tractor was explored in [28] using an electric machine with a single-reduction transmission ratio on each axle. The cruise axle features a permanent magnet synchronous machine (PMSM), which provides higher efficiency, higher torque density, and continuous power delivery. In contrast, the startability axle

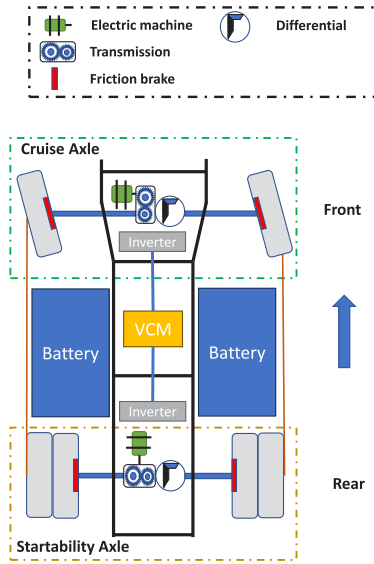


Fig. 2. Tractor and drivetrain configuration with cruise and startability axes. The VCM is a vehicle control module.

Table 1
Vehicle and environment parameters.

Parameters	value
Mass of the vehicle combination [kg], M_v	40 000
Mass of the Tractor [kg], M_T	17 100
Frontal area [m ²], A_v	9
Rolling resistance coefficient [-], C_{rr}	0.005
Drag coefficient [-], C_d	0.59
Wheel radius [m], $r_{w,1}$	0.47
Wheel radius [m], $r_{w,2}$	0.495
Air density [kg/m ³], ρ	1.2
Gravity constant [m/s ²], g	9.81
Battery capacity [kWh], E_{batt}	400
Front axle gear ratio [-], gr_1	12
PMSM max.continuous power [kW], $P_{maxEM,1}$	300
Road friction coefficient, μ	0.8
Rear axle gear ratio [-], gr_2	23
IM max. continuous power [kW], $P_{maxEM,2}$	300

uses an asynchronous induction machine (IM), which is slightly less efficient but more reliable, durable, and free from permanent magnet losses when idle [29]. The motivation to choose a distributed drivetrain topology with different electric machines is to exploit the over-actuation capabilities of the drivetrain to minimise power losses while achieving the traction requirements. The combination of PMSM on the cruise axle and IM on the startability axle also ensures a balance between cost, performance, and efficiency. The configuration of the electric machines on both axles, along with the selected gear ratios, was tailored to accommodate the entire vehicle's operating speed range. The specifications of the electric machines, gear ratios, and other vehicle parameters are shown in the Table 1. The electric machines were assumed to be controlled using one torque request for each, with the option to disconnect the IM inverter on demand. The wheels receive mechanical power from the drivetrain on each axle through a differential, and stiff shafts are assumed. Each wheel was configured with a friction brake actuator, including the semi-trailer.

4.2. Driving cycle

A section of the E20 highway route between Gothenburg-Alingsås in Sweden is chosen to evaluate the wheel torque coordination strategies. The driving cycle was extracted and post-processed using the information from Trafikverket's road database available in the VTM library 5.1

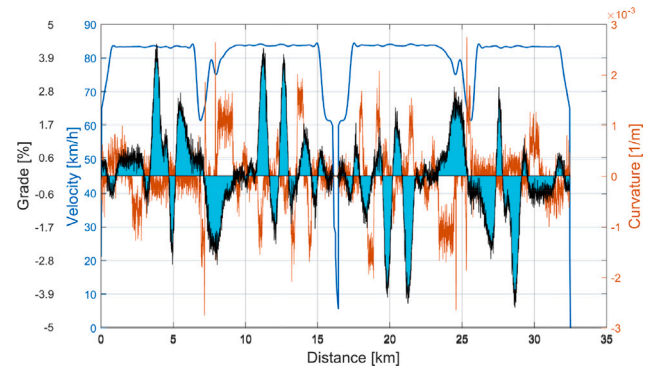


Fig. 3. Description of the driving cycle used in this study, showing a segment of long-haul heavy vehicle operation.

and used in the simulation model, with example results shown in Fig. 3. The driving cycle includes the topography, curvature, speed profile, and local road profiles in the longitudinal and lateral directions.

The original data from the database is limited to a distance of approximately 16.25 km. This distance is doubled by mirroring the data, and the vehicle is assumed to arrive at the starting point of the driving cycle. Using this simplification, a total distance of 32.5 km was used to define the driving cycle. The coefficient of friction between the tyre and road was assumed to represent the summer weather driving conditions on the tarmac and to be constant throughout the driving cycle.

5. Model for virtual verification

The system model is shown in Fig. 4 was developed and simulated using MATLAB[®]/Simulink[®]. To accelerate the simulation performance, a variable ODE solver (ODE45) was selected. In this study only the forward motion was considered. Furthermore, the friction brake usage of the trailer and hence the effect of the brake distribution between units, is not included in this study. In addition, no active control and safety functions were included in this analysis.

5.1. Vehicle dynamics

A high-fidelity vehicle model developed in-house by Volvo Group Trucks Technology using the Volvo Transport Models library (VTM) was used in this study [30]. The vehicle models within the VTM library are primarily modelled using multi-body dynamics and do not include drivetrain models. VTM is developed using MATLAB[®]/Simulink[®], Simscape[™]Multibody[™] and is used to simulate heavy vehicle dynamics. Heavy vehicle models in the VTM library were used for on-centre handling evaluations, control system development, and driving simulators. The VTM library has been validated using real test measurements and can be quickly adapted to suit different vehicle configurations. The default tyre models were developed using the PAC-2002 semi-empirical tyre model. The inputs to the VTM models are the wheel torque requests, steering wheel angle requests, and driving cycle inputs.

5.2. Driver model

The driver model uses the information of the drive cycle velocity profile, road gradient, and curvature as functions of the distance travelled. This information is used to generate virtual force requests for the actuator coordinator subsystem and steering wheel requests for the vehicle dynamics model. The virtual force requests to the actuator coordinator are then converted into wheel torque requests to achieve the desired vehicle motion. The driver model is composed of two parts: a longitudinal and lateral controller.

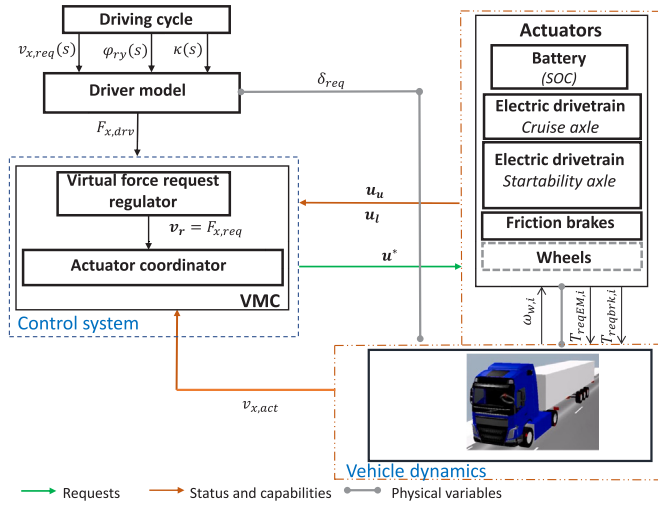


Fig. 4. Simplified representation of the simulation model showing the different subsystems and their interfaces.

5.2.1. Longitudinal control

The longitudinal controller was modelled to represent the cruise controller and follow the desired speed profile according to the defined driving cycle. This controller is designed to be adequate only for the specified driving cycle and needs improvement to handle complex scenarios. It is composed of a feed-forward and feedback part. The output sum $F_{x,drv}$ is requested by the actuator coordinator to maintain the desired vehicle speed.

The feed-forward controller is modelled using longitudinal vehicle dynamics model, as in (13), where $a_{x,req}$ represents the requested acceleration and is calculated as a time derivative of velocity request, $v_{x,req}$ at each instant.

$$F_{x,ff} = M_v \cdot a_{x,req} + F_{x,res} \quad (13)$$

The term $F_{x,res}$ represents the sum of all resistive forces applied to the vehicle motion.

$$F_{x,res} = \frac{1}{2} \cdot \rho \cdot C_d \cdot A_v \cdot v_{x,req}^2 + M_v \cdot g \cdot (C_r + \sin(-\varphi_{ry})) \quad (14)$$

To compensate for model errors in the feed-forward controller a simple proportional-based feedback controller was used. The feedback controller calculates the error of the actual vehicle velocity, $v_{x,act}$ against the velocity request, $v_{x,req}$ of the drive cycle. Using a gain factor of $k_b = \frac{1}{8} \cdot M_v$, the feedback force is calculated as:

$$F_{x,fb} = k_b \cdot (v_{x,req} - v_{x,act}) \quad (15)$$

$$F_{x,drv} = F_{x,fb} + F_{x,ff} \quad (16)$$

The feedback gain was adjusted through an iterative process of trial and error to achieve a steady state error within ± 0.1 m/s.

5.2.2. Lateral control

The lateral control part of the driver model is independent of the longitudinal controller and sends the steering wheel angle request, δ_{req} , to the wheels. Hence, the vehicle speed is not compensated according to the generated steering wheel inputs. This is a great simplification that requires treatment to handle critical and complex driving scenarios. One potential solution is to incorporate a driver interpreter and path controller, as demonstrated in [31]. In this study, such a simplification is justified to represent the scenario of driving with an active cruise controller for a less demanding driving cycle and high road-tyre friction.

The current controller which is available in the VTM library, was developed using a preview-based yaw tracking control strategy. The road curvature and vehicle states are fed to the driver model to produce the required output. A moderately selected driver setting is chosen and the parameters are adapted accordingly.

5.3. Vehicle motion controller

The Vehicle motion controller (VMC) has two main functions. The first step is to regulate the longitudinal force request from the driver model $F_{x,drv}$ and the second step to coordinate the regulated force request $F_{x,req} = v_r$, also called the virtual force request, as actuator force requests.

5.3.1. Virtual force request regulator

The virtual force request regulator limits the request $F_{x,drv}$ from the driver model using the capability limits of the actuators and the tractive force available on all wheels of the tractor unit. The information of the maximum and minimum force capability limits of the actuators u_u and u_l available at each instant are used to limit the force request from the driver model. Additionally, the force request is further saturated using the information of the total static load on the axles of the tractor and the road friction coefficient. The regulation process is described in (17) and it uses the maximum and minimum force capabilities of the actuators shown in Section 5.4. It is also important to note that the same limits must be applied to the optimisation algorithms to ensure feasibility.

$$v_r = \begin{cases} \max(\max(F_{x,drv}, \sum_p u_l(p)), -F_{xlim,T}), & \text{if } F_{x,drv} < 0 \\ \min(\min(F_{x,drv}, \sum_p u_u(p)), F_{xlim,T}), & \text{if } F_{x,drv} \geq 0 \end{cases} \quad (17)$$

where $F_{xlim,T} = \mu \cdot (M_T \cdot g)$ and p is the total number of actuators.

$$u_l = \begin{bmatrix} F_{xminEM,1} \\ F_{xminEM,2} \\ F_{xminbrk,1} \\ F_{xminbrk,2} \end{bmatrix}, u_u = \begin{bmatrix} F_{xmaxEM,1} \\ F_{xmaxEM,2} \\ F_{xmaxbrk,1} \\ F_{xmaxbrk,2} \end{bmatrix}$$

This simplified implementation is sufficient for managing the vehicle and its applications, as specified in this study. However, for driving situations involving high acceleration, evasive manoeuvres on low-friction surfaces and low-speed turning involving high steering wheel angles are not sufficient. To handle such cases, a driver interpreter, robust motion estimator, and wheel slip controllers are required. Such systems arranged in an hierarchical architecture, explored in [32–34], in achieving safe, efficient, and feasible requests.

5.3.2. Actuator coordinator

The main objective of the actuator coordinator is to map the virtual force request v_r to actuator requests. The coordinator uses information on vehicle configuration, actuator capabilities, vehicle states, and virtual force request v_r to produce the actuator requests. The Wheel torque coordination strategies presented in Section 6 are placed within this interface definition and are separately simulated.

5.4. Actuators

As the goal of this paper is to evaluate the performance of wheel torque coordination strategies, simplified models of actuators are utilised. However, by adapting of the defined signal interfaces, detailed actuator models can be easily added.

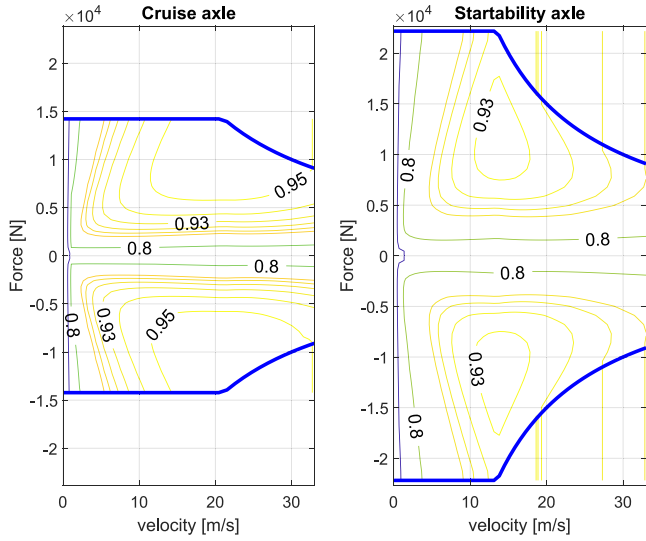


Fig. 5. Efficiency contours (labelled contour lines with efficiencies within the blue lines) and force limits ($F_{xmin,i}$ and $F_{xmax,i}$), represented by thick blue lines, of 300 kW electric machines; (left): Electric drivetrain on cruise axle; (right): Electric drivetrain on startability axle.

5.4.1. Electric drivetrain

The electric drivetrain on each axle includes models of the transmission losses, torque transfer dynamics, and capability calculation. The actuator models receive requests from actuator coordinators and receive the wheel speed status from the vehicle dynamics model to produce the required output. The torque transfer from the electric drivetrain to the wheels on each axle was modelled using a linear time-invariant system by introducing a time constant, $\tau_{EM} = 0.1$ s.

$$T_{EM,i} = \eta_{trmn,i} \cdot (T_{reqEM,i} - \tau_{EM} \frac{dT_{reqEM,i}}{dt}) \quad (18)$$

$$T_{reqEM,i} = F_{xreqEM,i} \cdot r_{w,i}$$

where $\eta_{trmn,i}$ is the efficiency definition given in (9), which is used to model the transmission losses on each axle. The torque request, $T_{reqEM,i}$, from each drivetrain is then distributed equally between the left and right wheels. Additionally, the power losses associated with the torque request were computed for each drivetrain using (26). In the case of a disconnected rear axle drivetrain, the IM power losses are limited to windage losses. This emulates a condition in which the inverter associated with the IM is turned off [28].

Furthermore, to obtain the force capability limits, the torque-rotational speed map of electric machines was modelled as lookup tables. The lookup table, representing a point-to-set mapping, was used to compute the minimum and maximum force capability limits of the electric machine on each axle at each instant and for a given vehicle speed, as in (19) and (20). The thick blue lines in Fig. 5, indicate the force capability limits of the electric machines on each axle.

$$F_{xminEM,i} = \min(F_{xEM,i}(v_{EM,i})) \quad (19)$$

$$F_{xmaxEM,i} = \max(F_{xEM,i}(v_{EM,i})) \quad (20)$$

where $v_{EM,j}$ is the translated speed of the electric machine on the axle, which is obtained using the relation.

$$v_{EM,i} = (v_{x,act}) \cdot g r_i \quad (21)$$

The capability limits are then transmitted to the actuator coordinator at each time step.

5.4.2. Friction brakes

At each instant, the brake force request from the actuator coordinator is transmitted to the respective brake actuators. The brake system was also simplified and modelled as a linear time-invariant system, and the output brake torque on each axle, which was distributed equally between the left and right wheels, was modelled as follows:

$$T_{brk,i} = T_{reqbrk,i} - \tau_{brk} \frac{dT_{reqbrk,i}}{dt} \quad (22)$$

$$T_{reqbrk,i} = F_{xreqbrk,i} \cdot r_{w,i}$$

The time constant of the brake torque output was set to $\tau_{brk} = 0.2$ s considering the delay in the pneumatic system and friction brake mechanism. Similar to electric machines, the brake actuator also relays the force capabilities of the brake actuator on each axle to the actuator coordinator, thus closing the loop as shown in Fig. 4

$$F_{xminbrk,i} = -2 \cdot 42.5 \text{ kN}, F_{xmaxbrk,i} = 0 \text{ kN}$$

5.4.3. Battery

The influence of the battery management system and the effects of battery dynamics on the energy storage and electrical power transmission were excluded. Thus, the battery is modelled as an energy storage system that accumulates and supplies electrical energy when requested. The battery power consumption $P_{Batt_{cons}}$ and regeneration $P_{Batt_{gen}}$ models are shown below, as in (23) and (24).

$$P_{Batt_{cons}} = \sum_i \left(\frac{P_{EM,i}}{\eta_{mot,i}} + P_{lossEM,i} \right) \quad (23)$$

$$P_{Batt_{gen}} = \sum_i (P_{EM,i} \cdot \eta_{gen,i} + P_{lossEM,i}) \quad (24)$$

$\eta_{mot,i} = 0.9$ and $\eta_{gen,i} = 0.85$ are the motoring and regenerating efficiencies. The term $P_{lossEM,i}$ indicates the power losses, and $P_{EM,i}$ is the mechanical power associated with the drivetrain. The power electronics losses of the inverters were also assumed to be constant and included in the defined battery efficiency parameters.

6. Wheel torque coordination strategies

This section compares three wheel torque coordination algorithms designed to enhance energy efficiency while preserving vehicle stability. The algorithms are intended for normal driving conditions and are anticipated to be supplemented by wheel slip control systems, such as anti-lock braking system (ABS) and electronic stability control systems (ESC), when necessary. However, during system activation, energy efficiency is not the primary consideration.

The fundamental principle underlying the first two algorithms presented is to minimise instantaneous power losses of the actuators. These two algorithms are then compared with a third algorithm that ensures equal utilisation of friction on all wheels. All algorithms were modelled as closed-loop systems, receiving feedback from actuators and vehicle states with full knowledge of the states.

The actuator coordination strategies are applicable to both the propulsion and braking torque requests. However, it is limited to the coordination of the electric drivetrains and friction brakes on the tractor. In addition, equal forces are assigned to the left and right wheels on each axle in each strategy. Finally, it is assumed that both electric drivetrains are operated for traction or regeneration on both axles and are optimal [21].

6.1. Power loss minimisation (PLM)

In the PLM algorithm, the main objective is to minimise the instantaneous power losses associated with the usage of electric machines and friction brakes while achieving the longitudinal motion request within the actuator and wheel force limits. As observed in Fig. 1, the

power losses of the chosen electric machines are nearly quadratic to the applied machine torque and linear for the friction brakes as in Section 3.5. Using this information, the actuator coordination task can be described as an optimisation problem.

The optimisation algorithm is expressed as follows:

$$\begin{aligned} \mathbf{u}^* &= \arg \left(\min_{\mathbf{u}} \left(\sum_i^m P_{lossEM,i} + \sum_i^m P_{lossbrk,i} \right) \right) \quad (25) \\ \text{s.t. } & B \cdot \mathbf{u} = \mathbf{v}_r \\ & \mathbf{u}_l \leq \mathbf{u} \leq \mathbf{u}_u \\ & -\mathbf{h} \leq G \cdot \mathbf{u} \leq \mathbf{h} \end{aligned}$$

where $m = 2$, for the given vehicle and control configuration. The minimisation of the tyre slip and rolling resistance losses was excluded in this problem formulation. The total force request to achieve the desired vehicle motion is expressed as an equality constraint, the wheel force limits as inequality constraints, and the actuator limits are expressed using box constraints. The quadratic nature of the power losses of the electric drivetrain along with linear equality and inequality constraints ensures that the problem is convex and that there exists a global minimum. Then, the algorithm then obtains numerical solutions to a constrained quadratic problem at every instant [28]. However, for higher order power losses, this method leads to a sub-optimal solution and requires a different treatment of the problem.

To numerically solve the quadratic problem, the power loss $P_{lossEM,i}$ of the electric machine is expressed as a second-order polynomial.

$$P_{lossEM,i} = a_{EM,i} \cdot T_{EM,i}^2 + b_{EM,i} \cdot T_{EM,i} + c_{EM,i} \quad (26)$$

where, $a_{EM,i}$, $b_{EM,i}$, and $c_{EM,i}$ are the curve fitting coefficients

The method and framework for extracting coefficients through regression for each instant and solving the optimisation problem is presented in [28]. However, in the present study, the overall simulation time is improved if these coefficients are extracted offline at the cost of some accuracy of the power loss information. Therefore, the power loss curves of both electric machines were curve-fitted on 50×50 grid data and stored as a look-up map. During the simulation, the coefficients are interpolated for intermediate operating points that are not defined in the grid.

Additionally, the equality constraint $B \cdot \mathbf{u} = \mathbf{v}_r$ ensures that the total longitudinal force request \mathbf{v}_r , as calculated in (17), achieves the desired vehicle motion. This is achieved by distributing \mathbf{v}_r as torque requests among the actuators. The term B in the equality constraint is referred to as the control effectiveness matrix, which indicates the number of active actuators and the effective capacity of each actuator to contribute to coordination. Similarly, the maximum and minimum force capability limits of the actuators, \mathbf{u}_u and \mathbf{u}_l , respectively, ensure that the individual actuator limits are not violated. Physically, these limits correspond to the maximum torque limits of the EMs and friction brakes for a given speed defined in (17), Sections 5.4.1 and 5.4.2.

In addition, to achieve safe driving performance, the lateral limits of each axle were determined. This limit is introduced as an inequality constraint to ensure that the lateral force limits on each axle are not violated when allocating the longitudinal forces. To calculate the lateral force limits on each axle, the normal loads $F_{z,i}$ and estimated lateral forces $F_{y,i}$ on each axle of the tractor unit at each instant were used along with the defined road friction coefficient. The matrix G consisting of 1's and 0's specifies the configuration of the actuators, electric machine, and friction brakes available on the axle. A detailed overview of the implementation of this constraint and some results are presented in [28].

$$\begin{aligned} -\mathbf{h} &\leq \left(\sum_i^m F_{xreqEM,i} + \sum_{i=1}^m F_{xreqbrk,i} \right) \leq \mathbf{h} \quad (27) \\ \mathbf{h} &= \sum_i^m F_{xlim,i} = \sum_i^m \sqrt{(\mu \cdot F_{z,i})^2 - (F_{y,i})^2} \end{aligned}$$

The representation given in (27) ensures that the wheel force limits are not violated during actuator coordination for the given vehicle specification and drive cycle.

The optimisation problem in (25), using (26), (27), and (12), is reformulated into a standard quadratic optimisation formulation as follows:

$$\begin{aligned} \mathbf{u}^* &= \arg \left(\min_{\mathbf{u}} \frac{1}{2} \mathbf{u}^T H \mathbf{u} + \mathbf{g}^T \mathbf{u} \right) \quad (28) \\ \text{s.t. } & B \cdot \mathbf{u} = \mathbf{v}_r \\ & \mathbf{u}_l \leq \mathbf{u} \leq \mathbf{u}_u \\ & G \cdot \mathbf{u} \leq \mathbf{h} \end{aligned}$$

where,

$$\begin{aligned} H &= 2 \cdot \begin{bmatrix} \frac{a_{EM,1} \cdot r_{w,1}^2}{g r_1^2} & 0 & 0 & 0 \\ 0 & \frac{a_{EM,2} \cdot r_{w,2}^2}{g r_2^2} & 0 & 0 \\ 0 & 0 & a_{brk,1} & 0 \\ 0 & 0 & 0 & a_{brk,2} \end{bmatrix} \\ \mathbf{g}^T &= \left[\frac{b_{EM,1} \cdot r_{w,1}}{g r_1}, \frac{b_{EM,2} \cdot r_{w,2}}{g r_2}, (-v_{xact,1}), (-v_{xact,2}) \right] \\ B &= [1 \quad 1 \quad 1 \quad 1], G = \begin{bmatrix} -1 & 0 & -1 & 0 \\ 0 & -1 & 0 & -1 \\ 1 & 0 & 1 & 0 \\ 0 & 1 & 0 & 1 \end{bmatrix} \\ \mathbf{v}_r &= F_{xreq}, \quad \mathbf{h} = \begin{bmatrix} F_{xlim,1} \\ F_{xlim,2} \\ F_{xlim,1} \\ F_{xlim,2} \end{bmatrix}, \quad \mathbf{u} = \begin{bmatrix} F_{xreqEM,1} \\ F_{xreqEM,2} \\ F_{xreqbrk,1} \\ F_{xreqbrk,2} \end{bmatrix} \end{aligned}$$

and $a_{brk,1} = a_{brk,2} = 1e^{-5}$.

The terms $v_{xact,1}$ and $v_{xact,2}$ represent the longitudinal velocities of the axle, and $a_{brk,1}$ and $a_{brk,2}$ are numerical constants used to make the hessian H positive definite for quadratic programming.

The quadratic problem was solved at each time step using the MATLAB[®] *quadprog* solver. The output from the optimisation was converted into wheel torque requests using the actuator model. Note that G effectively becomes a matrix with entries of ternary number, i.e. $-1, 0$, and 1 , indicating the actuators available to achieve the motion request and also indicates the configuration of actuators on the vehicle.

Finally, it is important to note that, in a standard quadratic programming formulation, the constant term $c_{EM,i}$ from the curve fitting, is neglected because it does not influence \mathbf{u}^* . Thus it is assumed that the measure of idle losses of the electric machines is excluded from the actuator coordination. In other words, the implementation of using a clutch or switching the drivetrain electrically cannot be captured using a quadratic program. Thus, the algorithm always finds a solution that coordinates requests between actuators on both axes.

6.2. Power loss minimisation including idle losses (ILPLM)

The principle in this strategy is to include the influence of the constant term $c_{EM,i}$ in (26) representing the idle losses (power loss at zero torque) while coordinating the actuators. Fig. 1 shows that the idle losses are higher for the IM at all speeds compared to the PMSM. Hence, to account for the idle losses of the IM, wheel torque allocation is performed by comparing the power losses of the PLM method, the idle losses of the PMSM, and the friction brakes on the startability axle. The simplified logic flow of the ILPLM algorithm is seen in Fig. 6. The ILPLM algorithm operates by refining the outputs from quadratic programming using condition statements, thereby treating the $c_{EM,i}$ term.

The decision nodes in the logical flow chart of Fig. 6 compare the power losses in the PLM algorithm with the power losses excluding IM. The following steps were followed to achieve optimal wheel torque coordination:

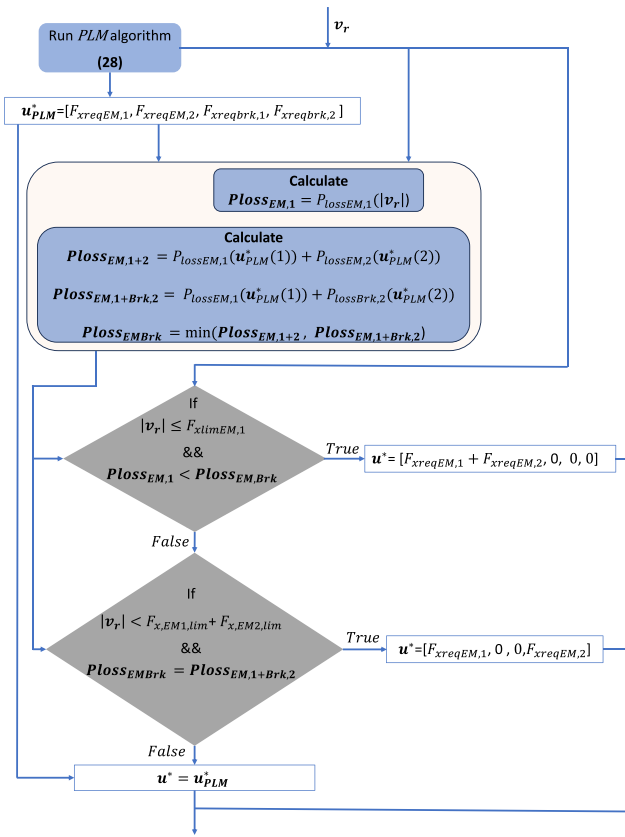


Fig. 6. Logical flow chart of the *ILPLM* algorithm for optimal actuator coordination.

- The *PLM* algorithm is evaluated at every instant, and the output is used to calculate the power losses of the electric machines using the curve fitting coefficients.
- Using the outputs from the *PLM* power losses of the combination of the PMSM, IM and friction brake on startability axle is computed.
- The force request $F_{x,req}$ used in the *PLM* computation is parallelly checked if it is within the cruise axle force limits (minimum of wheel and PMSM limit). Additionally, the power losses associated with operating the PMSM, is compared with those of the sum of the PMSM and friction brake on the startability axle. If the power loss of PMSM is lower and if force request is feasible, the force request is forwarded to the PMSM.
- If the force request is above the capability limits of the PMSM, then a similar check is made by comparing with the sum of the cruise and startability axle force limits. Simultaneously, an extra feature was added to the *ILPLM* algorithm by considering the possibility of using friction brakes on the startability (rear) axle if it is power loss optimal, as shown in Fig. 6. If the calculated power loss when using the PMSM and friction brakes on the startability axle is less than the power loss with the use of the PMSM and IM, then the PMSM and friction brakes are recommended. Otherwise, the request is forwarded to the *PLM* algorithm and the respective actuators.

Fig. 7, shows the power losses associated with the *ILPLM* and *PLM* algorithms for the operation points achievable by only using electric machines. When friction brakes are used, a wider range of operating forces is possible. The contour levels highlight the optimal power losses associated with the operation of the actuators in each algorithm. As mentioned for the *ILPLM*, friction brakes can be used on the startability axle. The red curves in the upper subplot of Fig. 7

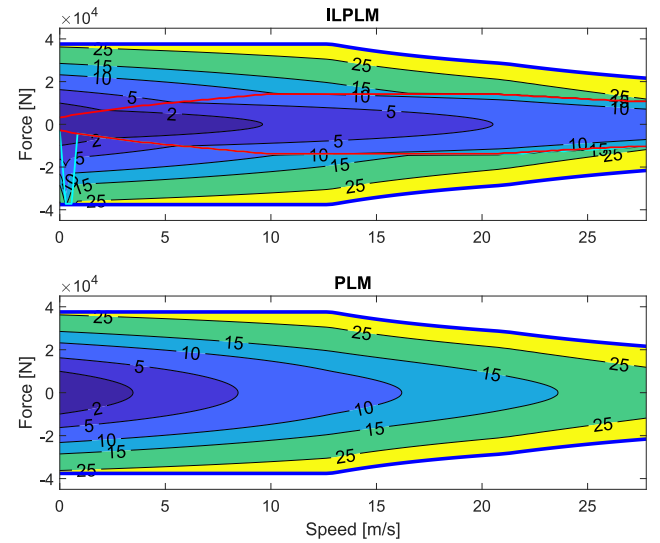


Fig. 7. Contour of power losses obtained using the *ILPLM* and *PLM* algorithms, represented using the force v/s velocity diagram. The contour levels represent the power losses associated with the operating electric machines and friction brakes in the case of the *ILPLM* and without friction brakes for the *PLM*. The blue thick lines represent the limits of the total maximum force achieved using only the drivetrains. The contour level values are expressed in kW. In the upper subplot, the area between the red curves represents where it is optimal to demagnetise the startability axle drivetrain. Furthermore, a similar region enclosed between the lower red and cyan curves, shows where it is optimal to use friction brakes instead of electric machines on the startability axle.

represent the boundary between the two operating modes. The region within the red curves, also referred to as switching curves in literature, indicate the operating points achieved using only the electric drivetrain on the cruise axle. Therefore, for lower force requests, it is optimal to allocate all the forces to the cruise axle drivetrain. This result can be further verified by comparing the contour levels of the *PLM* and *ILPLM* algorithms. Furthermore, a similar region enclosed between the lower red and cyan curves, shows where it is optimal to use friction brakes, in addition to the front axle drivetrain, instead of electric machines on the startability axle. Fig. 7 also shows that this region is not significant at higher speeds and is usually efficient at very low speeds. Hence, this region was excluded from the *ILPLM* algorithm. Finally, in the regions outside these switching curves or boundaries, the power losses are similar to those of the *PLM* algorithm and confirm the operation of the electric drivetrains on both axles. The characteristic of the switching line depends on the following:

- performance characteristics and electric machine type.
- different sources of losses included for optimisation.
- hysteresis characteristics for safe, reliable, and smooth actuator operation.

6.3. Equal friction utilisation (EFU)

To evaluate the performance of power loss minimisation-based wheel torque allocation strategies, a method commonly used in brake force distribution is introduced. In principle, this strategy ensures the equal utilisation of tyre road friction on each wheel, depending on the normal loads on each axle. The relationship between the axles to ensure equal friction is defined as follows:

$$\frac{F_{x,1}}{\mu F_{z,1}} = \frac{F_{x,2}}{\mu F_{z,2}} \quad (29)$$

where $F_{x,1}$ is the longitudinal force, and $F_{z,1}$ is the axle load on the first axle, and $F_{x,2}$ and $F_{z,2}$ are the axle loads on the second axle. Thus, the

Algorithm 1 Pseudo code to compute u^* for EFU

```

if ( $F_{x,req} >= 0$ ) then
  if  $F_{xreq,2} > \min(F_{xmaxEM,2}, F_{xlim,2})$  then
     $F_{xreqEM,1}^* = \min(\min(F_{xmaxEM,1}, F_{xlim,1}),$ 
       $(F_{xreq,1} + (F_{xreq,2} - \min(F_{xmaxEM,2},$ 
         $F_{xlim,2}))))$ ;
  else
     $F_{xreqEM,1}^* = \min(F_{xreq,1}, \min(F_{xmaxEM,1},$ 
       $F_{xlim,1}))$ ;
  end if
  if  $F_{xreq,1} > \min(F_{xmaxEM,1}, F_{xlim,1})$  then
     $F_{xreqEM,2}^* = \min(\min(F_{xmaxEM,2}, F_{xlim,2}),$ 
       $(F_{xreq,2} + (F_{xreq,1} - \min(F_{xmaxEM,1},$ 
         $F_{xlim,1}))))$ ;
  else
     $F_{xreqEM,2}^* = \min(F_{xreq,2}, \min(F_{xmaxEM,2},$ 
       $F_{xlim,2}))$ ;
  end if
   $F_{x,brk11,req}^* = 0, F_{x,brk21,req}^* = 0$ 
else
  if  $F_{xreq,2} > \min(\text{abs}(F_{xminEM,2} + F_{xminbrk,2}), F_{xlim,2})$  then
     $F_{xreqEM,1}^* = \min(\min(\text{abs}(F_{xminEM,1} + F_{xminbrk,1}), F_{xlim,1}), (F_{xreq,1} +$ 
       $(F_{xreq,2} - \min(\text{abs}(F_{xminEM,2} + F_{xminbrk,2}), F_{xlim,2}))))$ ;
  else
     $F_{xreqEM,1}^* = \min(F_{xreq,1}, \min(\text{abs}(F_{xminEM,1}$ 
       $+ F_{xminbrk,1}), F_{xlim,1}))$ ;
  end if
  if  $F_{xreq,1} > \min(\text{abs}(F_{xminEM,1} + F_{xminbrk,1}), F_{xlim,1})$  then
     $F_{xreqEM,2}^* = \min(\min(\text{abs}(F_{xminEM,2} + F_{xminbrk,2}), F_{xlim,2}), (F_{xreq,2} +$ 
       $(F_{xreq,1} - \min(\text{abs}(F_{xminEM,1} + F_{xminbrk,1}), F_{xlim,1}))))$ ;
  else
     $F_{xreqEM,2}^* = \min(F_{xreq,2}, \min(\text{abs}(F_{xminEM,2}$ 
       $+ F_{xminbrk,2}), F_{xlim,2}))$ ;
  end if
   $F_{xreqEM,1}^* = \text{sgn}(F_{x,req}) * \min(F_{xreqEM,1},$ 
     $\text{abs}(F_{xminEM,1}))$ 
  if  $\text{sgn}(F_{x,req}) * (F_{xreqEM,1}) < F_{xminEM,1}$  then
     $F_{xreqbrk,1}^* = (\text{sgn}(F_{x,req}) * F_{xreqEM,1}) - F_{xreqEM,1}^*$ 
  else
     $F_{xreqbrk,1}^* = 0$ 
  end if
  if  $\text{sgn}(F_{x,req}) * (F_{xreqEM,2}) < F_{xminEM,2}$  then
     $F_{xreqbrk,2}^* = (\text{sgn}(F_{x,req}) * F_{xreqEM,2}) - F_{xreqEM,2}^*$ 
  else
     $F_{xreqbrk,2}^* = 0$ 
  end if
end if

```

total longitudinal force request from the driver can be fulfilled through axle force requests.

$$F_{x,req} = F_{xreq,1} + F_{xreq,2} \quad (30)$$

Using Eqs. (29) and (30), the force request on each axle can be expressed as:

$$F_{xreq,1} = \frac{F_{z,1}}{F_{z,1} + F_{z,2}} \cdot F_{x,req} \quad (31)$$

$$F_{xreq,2} = F_{x,req} - F_{xreq,1} \quad (32)$$

where $F_{xreq,1}$ and $F_{xreq,2}$ are the axle force requests. However, when the request for an actuator force exceeds the available wheel force limits, the surplus request is transferred to the other axle. In addition, as a

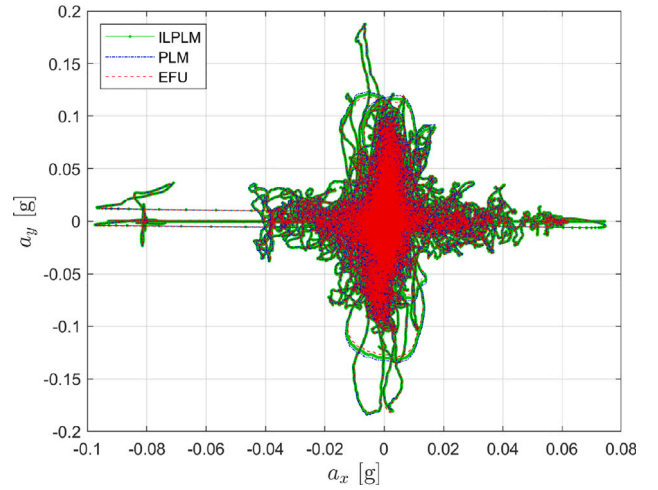


Fig. 8. Plot of longitudinal acceleration versus lateral acceleration measured at centre of gravity (CoG) of vehicle. These measures were obtained from the vehicle model while traversing the given driving cycle for the three wheel torque allocation strategies.

rule, the electric machines on each axle are prioritised to achieve the axle force requests until they are saturated by their capability limits. The remaining axle force was compensated using friction brakes on each axle. The logical flow of the proposed EFU strategy is presented in algorithm 6.3.

7. Simulation results

This section provides a comparative evaluation of the simulation outcomes of various wheel torque allocation strategies. Two key performance indicators, driving performance and energy consumption, were employed to assess the effectiveness of each wheel torque allocation strategy. Prior to the detailed analysis, it was verified that both the tractor and the trailer remained within the lane throughout the driving cycle. This validation was conducted to ensure a fair comparison and to preclude any potential issues that could influence the results. The validation process involved monitoring the position of the tractor and the trailer at regular intervals throughout the driving cycle. Furthermore, the time taken to complete the entire driving cycle was evaluated to establish a baseline for the performance metrics. The results indicate that the time required to complete the driving cycle for each strategy differs insignificantly, with variations of less than 0.5 s. These minor discrepancies are considered acceptable for the comparison of heavy vehicle operations, as per engineering judgment. The small differences in completion time are attributed to the distinct dynamics resulting from different actuator coordination strategies, stopping criteria, and numerical integration methods.

The optimisation problem in *PLM* and *ILPLM* was resolved using the *quadprog* solver in conjunction with the *active-set* algorithm. Throughout the simulation, the optimisation solver consistently converged to a solution, achieving this within a maximum of 7 iterations and a maximum condition number of 12. The condition number of 12 indicates that the problem was reasonably well-conditioned, thereby facilitating the attainment of accurate and stable solutions. The solver was unable to identify further improvements, and the obtained solutions complied with the specified tolerance levels. As a result, the solver is capable of identifying the optimal solutions within the given constraints.

7.1. Driving performance

This section presents the lateral and longitudinal responses of vehicle models for wheel torque coordination strategies. Fig. 8 illustrates

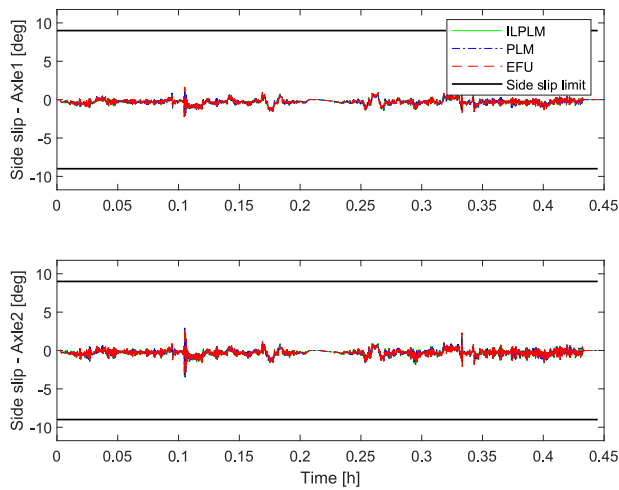


Fig. 9. Lateral slip of the front and the rear axle of the tractor in the wheel coordinate system and translated to the axle centre on ground. The side slip limits indicate threshold of lateral force saturation on each axle for the high road friction.

the plot of longitudinal versus lateral acceleration responses, also referred to as the g-g diagram [35]. The plot demonstrates the vehicle model performance throughout the entire driving cycle for the three coordination strategies. In all instances, the lateral acceleration levels are within ± 0.2 g, while the longitudinal acceleration is limited within ± 0.1 g. These findings confirm that the selected driving cycle represents a long-haul driving cycle with mild conditions and no extreme manoeuvres. The similarity of the acceleration levels also validates the normal driving behaviour of the driver model and the consistency of the remaining system models, excluding the wheel torque coordination algorithms. Furthermore, the acceleration levels for high-friction surfaces indicate that the force margins (27) on the wheels are not violated and have sufficient margin.

The side slip on the front and rear axles of the tractor unit, a critical indicator of vehicle stability, was also examined. Fig. 9 illustrates the side slip on the front and rear axles of the tractor unit throughout the entire driving cycle. The side-slip levels on the axles remained well within established limits, which serve as indicators of axle force saturation. Exceeding these limits would signify vehicle instability, a scenario not encountered in the given transport application or coordination strategies. The results revealed no substantial differences among the various coordination strategies. Notable peaks were observed in the results for all cases, primarily resulting from road profile variations that induce disturbances, leading to aggressive steering-wheel angle corrections. Upon closer inspection of the side slip values, the rear axle slips exhibited slightly higher values, suggesting slightly oversteering behaviour at the peaks caused by road surface variations. This behaviour is attributed to the influence of the trailer, which transfers forces through the fifth wheel coupling located near the rear axle. This phenomenon was observed across all coordination strategies, emphasising the need to consider the vehicle design and configuration in a given application. However, in regions with slow speeds and minimal road profile variations, the vehicle exhibited slightly understeer behaviour. Consequently, it can be concluded that all strategies perform reasonably well in terms of stability. Furthermore, through detailed examination, extremely small differences in the order of 10^{-3} were observed at the peaks in the case of *ILPLM*, which quickly dissipated. These overshoots are deemed insignificant in the current application.

Additionally, the analysis of driver comfort was conducted in conjunction with vehicle handling performance. The primary objective was to evaluate the longitudinal comfort resulting from the torque coordination between the axles. The results, presented in Fig. 10, utilised longitudinal acceleration of tractor chassis sampled at 10 ms intervals

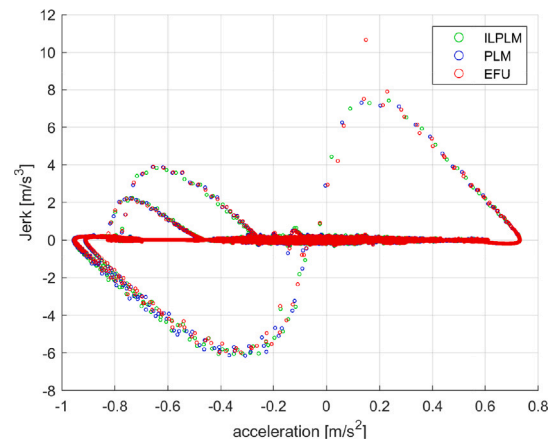


Fig. 10. Plot of longitudinal jerk versus longitudinal acceleration: a metric to assess driver comfort as a result of wheel torque coordination.

to calculate the jerk values for the specified transport application. The findings indicate that jerk levels for most driving durations fell within 2 m/s^3 , which is a benchmark for comfort [36,37]. These levels also validate the normal driving behaviour of the driver model under highway conditions. However, during acceleration and braking phases, higher jerk values were observed. Although elevated, these values can be considered within acceptable limits. Consequently, no significant differences were noted in driver comfort, and the coordination strategies performed uniformly. Furthermore, the velocity profile or acceleration request to the coordination strategies can be regulated to limit jerk levels, which were not considered in this study. It is also seen that the road profile variations can induce disturbances in conjunction with the aforementioned effects, as road irregularities can cause the vehicle to experience sudden changes in acceleration, potentially leading to higher jerk values. Therefore, a separate analysis focusing on driver comfort is necessary, along with subjective testing, which is a topic for further research related to wheel torque coordination.

7.2. Energy consumption

In this section, the energy consumption of the coordination strategies for the transport application are presented. The battery energy consumption of the three strategies during the driving cycle are shown in Fig. 11. The energy consumption was measured as the total accumulated motion power and power losses of the electric drivetrain, including the conversion losses and friction brake losses over time. The *ILPLM* strategy had the lowest energy consumption, followed by the *PLM* strategy and then the *EFU* strategy. The *ILPLM* strategy resulted in 7% lower energy consumption than the *EFU* strategy. The battery energy consumption remained the same for all the cases until 0.1 h and then started to diverge. This is noticed when both the cruise and startability axles are used to their limits during the acceleration of the vehicle to the required speed. Once the cruising speed is reached according to the drive cycle, which is also associated with low-torque requirements, the *ILPLM* coordination strategy deactivates the IM. However, in the other two cases, both the drivetrains are active, producing higher losses. This result is observed at the time mentioned, where the deviation on the energy curve is seen in Fig. 11. Thus, the result also verifies the claim that configuring an IM on the startability axle and electrically disconnecting it helps reduce the energy consumption. The energy consumption did not vary significantly between the *PLM* and *EFU*, with the *PLM* being slightly more efficient, showing a difference of less than 0.5%. The small difference observed can be attributed to the factors such as the driving cycle, friction coefficient and vehicle configuration influencing the vertical loads on the axles.

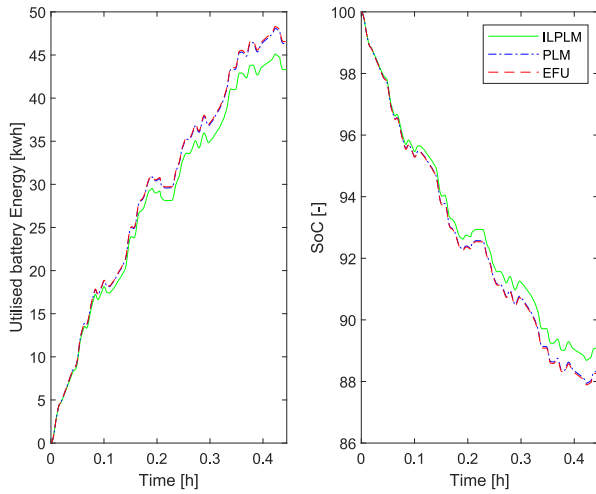


Fig. 11. Energy consumption and battery SoC levels in three-wheel torque allocation strategies and the given use case.

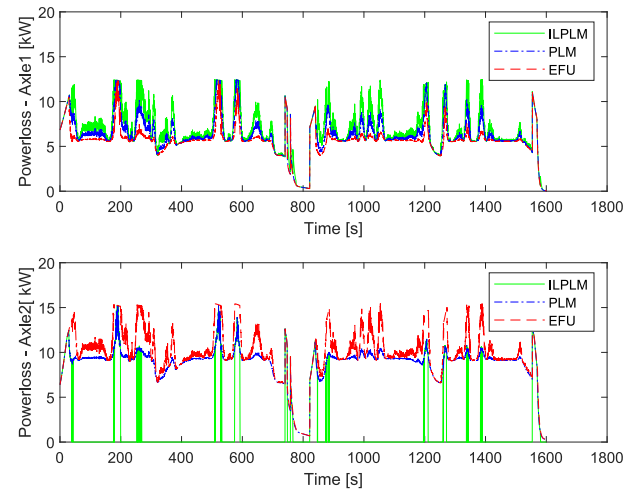


Fig. 13. Power loss on each axle versus time for wheel torque allocation strategies over a driving cycle.

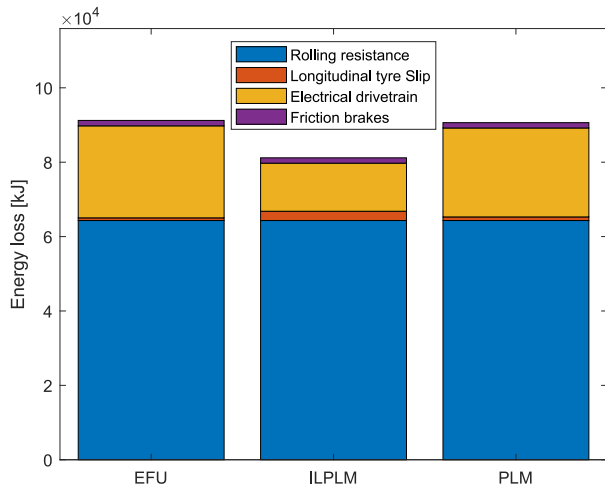


Fig. 12. Energy consumed by different sources in the three wheel torque allocation strategies. The levels can also be compared with the total consumed energy around 45 kWh = 16.2×10^4 kJ from Fig. 9.

Additionally, to compare the performance between the allocation strategies, the energy contributions from different power loss sources for the entire driving cycle are recorded as highlighted in Fig. 12. The results show that the *ILPLM* exhibited the lowest energy consumption because of the reduced power losses from the drivetrain. However, for the *PLM* and *EFU* strategies, the drivetrain losses were approximately the same and exceeded those of the *ILPLM* strategy. It is important to recall that only the power losses associated with the drivetrain and friction brake usage are minimised in the case of the *PLM* and *ILPLM*. The rolling resistance and longitudinal slip losses presented here are the consequences of the wheel torque allocation. In particular, the rolling resistance for the entire vehicle combination (tractor and semi-trailer together) was recorded, and hence, the contribution looks higher. The friction brake losses are also approximately the same in all cases and they are mainly active during the high deceleration requirements seen in Fig. 3.

From the presented result, it can be inferred that the active control of the drivetrain considering the disconnecting the IM significantly influences the energy consumption. This assertion is supported by Fig. 13, which illustrates the power losses of both the front and rear axle drivetrains throughout the driving cycle. In the case of the *ILPLM*,

the rear-axle drivetrain is electrically disconnected (without using mechanical clutches) for a prolonged period, thereby minimising the idle losses. The results confirm that the longitudinal force request $F_{x,req}$ predominantly falls within the region between the red curves in Fig. 7. Furthermore, the results also reflect the trend of the torque produced by the electric machines in Fig. 13. It was observed that for certain durations, the frequency of disconnection and reconnection was higher, which can generate undesirable driveline oscillations. Previous research [18,19] has shown that the trade-off between switching frequency and power consumption can be addressed by incorporating a switching cost into the cost function used in the optimisation. Alternatively, introducing a minimum time between switches while respecting longitudinal force requests and utilising heuristics or predictive control, can be implemented to mitigate the frequent switching problem. Furthermore, this problem is considered as a tuning task and is not explored in detail in the present study. Hence, the energy consumption results presented represent an ideal scenario, which would be higher if the switching hysteresis characteristics were included. Consequently, to balance vehicle performance, comfort, and efficiency, it is essential to consider hysteresis losses and the durability of power electronic components.

Furthermore, disconnecting the drivetrain on the startability axle increased the utilisation of the front axle drivetrain, requiring higher slip from the front axle tyres to meet the force demand. Thus, the direct influence of wheel torque allocation on longitudinal slip is evident as seen in Fig. 12, with a higher penalty observed in the case of the *ILPLM* strategy. In contrast, the *PLM* and *EFU* strategies exhibited minimal slip energy losses because of the distribution of the force requests between the axles. This illustrates the additional cost of minimising power losses through single-axle allocation and underscoring the need to incorporate slip losses (proportional to tyre wear) or total operating costs when developing wheel coordination strategies.

Another important reason for observing axle slip is to ensure safe vehicle performance. Although, the *ILPLM* saved significant energy in the tested application, friction constraints were not activated due to high-friction conditions. However, the *ILPLM* strategy's tendency to induce higher slip on one axle, particularly the front axle, requires adjustments of the axle force to maintain vehicle stability. This is especially important on low-friction surfaces or during high longitudinal and lateral acceleration. In such scenarios, the motion states must be monitored, and additional control is required to prevent the stability margins from becoming too low. For example, the side-slip at each axle should be tracked. Additionally, when a stability controller intervenes to ensure stability, energy consumption will no longer be

minimised. In these situations, the priority shifts from energy efficiency to maintaining stability. Hence, a wider range of operating conditions, such as lower road friction, should be tested in future research to better understand the *ILPLM* algorithm's performance under varying conditions.

Finally, in the case of rolling resistance losses, no significant difference was observed between the strategies for the specific application, primarily due to simple rolling resistance chosen. Without the consideration of the tyre operating temperature in the rolling resistance model. With a sophisticated rolling resistance model that includes the thermal and variations in the energy consumption are expected for different coordination algorithms.

8. Conclusion

In this study, three strategies for wheel torque allocation were analysed using simulations on a heavy vehicle with a drivetrain distributed on multiple axles. Two of the three strategies, *PLM* and *ILPLM*, use the principle of optimisation-based control allocation. Optimisation problem formulations are presented to minimise the power losses of electric machines and friction brakes while achieving motion requests and respecting wheel force limits. The third strategy called the *EFU* maximises the tyre grip, ensuring equal friction utilisation on both axles. A distributed drivetrain concept using two different types of electric machines, PMSM and IM, one on each axle is also introduced. Next, a comprehensive simulation framework is developed to verify the allocation strategies using a high-fidelity vehicle model, and real driving cycle data is developed. The optimal wheel-torque allocation is described by a quadratic program, and the wheel torques are allocated instantaneously at each time step.

The simulation results show that the *ILPLM* strategy is 7% and the *PLM* strategy is 0.5% more energy-efficient than the *EFU* strategy for the given use-case. In the *ILPLM* strategy, idle losses and the *PLM* algorithm outputs are utilised in the decision logic to minimise the power losses. Simple conditional statements are used to overcome the deficiency of not treating the constant term in the standard quadratic program formulation. The proposed method provides an advantage over mixed-integer quadratic programming for such problems and facilitates real-time application. The solution obtained from the *ILPLM* strategy demonstrates that it is efficient to operate a single drivetrain (front axle) in a distributed drivetrain configuration. Thus, the potential of IMs to not induce magnetisation losses in the stator when inactive is exploited using the *ILPLM* strategy. Such an optimal strategy also helps to minimise drag losses, avoid the use of mechanical clutches, and can be easily extended to other machines not using permanent magnets. However, the results also show that this leads to increased longitudinal tyre slip losses on the front axle.

These strategies were only verified conceptually; thus, they need to be explored for different driving cycles, road conditions, and vehicle configurations to evaluate their effectiveness. Additionally, other objectives like tyre wear, which is directly proportional to the tyre slip and rolling resistance losses, can be included in the objective function for optimisation to consider the holistic transportation cost of operation. Detailed actuator models, including thermal models and the hysteresis of actuators, power electronics, and electrical systems, are needed to improve the precision of the energy consumption results. For vehicles with more than two driven axles, the *ILPLM* strategy must be reformulated as a mixed integer optimisation problem rather than conditional statements.

CRedit authorship contribution statement

Sachin Janardhanan: Writing – original draft, Visualization, Software, Funding acquisition, Formal analysis, Conceptualization. **Leon Henderson:** Writing – review & editing, Supervision, Conceptualization. **Mats Jonasson:** Writing – review & editing, Supervision, Conceptualization. **Bengt Jacobson:** Writing – review & editing, Supervision,

Project administration, Funding acquisition, Conceptualization. **Esteban R. Gelso:** Writing – review & editing, Supervision, Software, Conceptualization.

Declaration of competing interest

The authors declare the following financial interests/personal relationships which may be considered as potential competing interests: Sachin Janardhanan reports financial support was provided by Volvo Technology AB. Sachin Janardhanan reports a relationship with Volvo Technology AB that includes: employment. Leon Henderson reports a relationship with Volvo Technology AB that includes: employment. Esteban R. Gelso reports a relationship with Volvo Technology AB that includes: employment. If there are other authors, they declare that they have no known competing financial interests or personal relationships that could have appeared to influence the work reported in this paper.

Acknowledgement

The results from this article is part of research project funded by Swedish Energy Agency and Volvo Group, Sweden.

Data availability

Data will be made available on request.

References

- [1] F. Rodriguez, O. Delgado, R. Muncrief, Fuel consumption testing of tractor-trailers in the European Union and the United States, 2018, URL www.gpo.gov/fdsys/pkg/FR-2011-09-15/.
- [2] T. Earl, L. Mathieu, S. Cornelis, S. Kenny, C.C. Ambel, J. Nix, Analysis of long haul battery electric trucks in EU Marketplace and technology, economic, environmental, and policy perspectives. European Federation for Transport and Environment, 2018, URL <https://ec.europa.eu/inea/en/ten-t/ten-t-projects>.
- [3] B. Djordjevic, B. Ghosh, Estimation of emissions and fuel consumption from Irish HDVs using VECTO tool, Transp. Res. Procedia 72 (2023) 3825–3831, <http://dx.doi.org/10.1016/j.trpro.2023.11.505>, TRA Lisbon 2022 Conference Proceedings Transport Research Arena (TRA Lisbon 2022), 14th–17th November 2022, Lisboa, Portugal, URL <https://www.sciencedirect.com/science/article/pii/S2352146523008037>.
- [4] B.O. Varga, A. Sagoian, F. Mariasiu, Prediction of electric vehicle range: A comprehensive review of current issues and challenges, Energies 12 (2019) <http://dx.doi.org/10.3390/en12050946>.
- [5] E.M. Szumska, R.S. Jurecki, Parameters influencing on electric vehicle range, Energies 14 (2021) <http://dx.doi.org/10.3390/en14164821>.
- [6] A. Sforza, B. Lenzo, F. Timpone, A state-of-the-art review on torque distribution strategies aimed at enhancing energy efficiency for fully electric vehicles with independently actuated drivetrains, Int. J. Mech. Control. 20, URL <http://shura.shu.ac.uk/25806/>.
- [7] D. Wang, C. Guan, J. Wang, H. Wang, Z. Zhang, D. Guo, F. Yang, Review of energy-saving technologies for electric vehicles, from the perspective of driving energy management, Sustainability 15 (9) (2023) <http://dx.doi.org/10.3390/su15097617>, URL <https://www.mdpi.com/2071-1050/15/9/7617>.
- [8] L. Laine, J. Fredriksson, Coordination of vehicle motion and energy management control systems for wheel motor driven vehicles, in: 2007 IEEE Intelligent Vehicles Symposium, 2007, pp. 773–780, <http://dx.doi.org/10.1109/IVS.2007.4290210>.
- [9] J. Torinsson, M. Jonasson, D. Yang, B. Jacobson, Energy reduction by power loss minimisation through wheel torque allocation in electric vehicles: a simulation-based approach, Veh. Syst. Dyn. (2020) 1–24, <http://dx.doi.org/10.1080/00423114.2020.1858121>.
- [10] G. De Filippis, B. Lenzo, A. Sorniotti, P. Gruber, W. De Nijs, Energy-efficient torque-vectoring control of electric vehicles with multiple drivetrains, IEEE Trans. Veh. Technol. 67 (6) (2018) 4702–4715, <http://dx.doi.org/10.1109/TVT.2018.2808186>.
- [11] C. Chatzikomis, M. Zanchetta, P. Gruber, A. Sorniotti, B. Modic, T. Motaln, L. Blagotinsk, G. Gotovac, An energy-efficient torque-vectoring algorithm for electric vehicles with multiple motors, Mech. Syst. Signal Process. 128 (2019) 655–673, <http://dx.doi.org/10.1016/j.ymsp.2019.03.012>, URL <https://www.sciencedirect.com/science/article/pii/S0888327019301657>.

- [12] A.M. Dizqah, B. Lenzo, A. Sorniotti, P. Gruber, S. Fallah, J. De Smet, A fast and parametric torque distribution strategy for four-wheel-drive energy-efficient electric vehicles, *IEEE Trans. Ind. Electron.* 63 (7) (2016) 4367–4376, <http://dx.doi.org/10.1109/TIE.2016.2540584>.
- [13] M. Dalboni, G. Martins, D. Tavernini, U. Montanaro, A. Soldati, C. Concarì, M. Dhaens, A. Sorniotti, On the energy efficiency potential of multi-actuated electric vehicles, *IEEE Trans. Veh. Technol.* (2024) 1–16, <http://dx.doi.org/10.1109/TVT.2024.3378154>.
- [14] S. Salamone, B. Lenzo, G. Lutzemberger, F. Bucchi, L. Sani, On the investigation of energy efficient torque distribution strategies through a comprehensive powertrain model, *Sustainability* 13 (8) (2021) <http://dx.doi.org/10.3390/su13084549>, URL <https://www.mdpi.com/2071-1050/13/8/4549>.
- [15] A. Pennycott, L.D. Novellis, P. Gruber, A. Sorniotti, T. Goggia, Enhancing the energy efficiency of fully electric vehicles via the minimization of motor power losses, in: 2013 IEEE International Conference on Systems, Man, and Cybernetics, 2013, pp. 4167–4172, <http://dx.doi.org/10.1109/SMC.2013.710>.
- [16] J. Hu, J. Li, Z. Hu, B. Zhang, L. Xu, M. Ouyang, Energy-efficient torque-allocation strategy for a 6×6 vehicle using electric wheels, *eTransportation* 10 (2021) 100136, <http://dx.doi.org/10.1016/j.etrans.2021.100136>, URL <https://www.sciencedirect.com/science/article/pii/S2590116821000345>.
- [17] Y. Xu, A. Kersten, S. Klacar, B. Ban, J. Hellsing, D. Sedarsky, Improved efficiency with adaptive front and rear axle independently driven powertrain and disconnect functionality, *Transp. Eng.* 13 (2023) 100192, <http://dx.doi.org/10.1016/j.treng.2023.100192>, URL <https://www.sciencedirect.com/science/article/pii/S2666691X23000325>.
- [18] S. Koehler, A. Viehl, O. Bringmann, W. Rosenstiel, Energy-efficient torque distribution for axle-individually propelled electric vehicles, in: 2014 IEEE Intelligent Vehicles Symposium Proceedings, 2014, pp. 1109–1114, <http://dx.doi.org/10.1109/IVS.2014.6856499>.
- [19] G. Ivo, B. Škugor, J. Deur, Energy-efficient straight-line driving torque vectoring for electric vehicles with disconnect clutches and unequal front/rear motors, in: 16th International Symposium on Advanced Vehicle Control, Springer Nature Switzerland, Cham, 2024, pp. 364–370.
- [20] G. Bingzhao, Y. Yongjun, C. Hong, C. Hong, X. Nan, Torque allocation of four-wheel drive EVs considering tire slip energy, *Sci. China Inf. Sci.* 65 (2021) <http://dx.doi.org/10.1007/s11432-019-2946-8>.
- [21] B. Lenzo, G. De Filippis, A.M. Dizqah, A. Sorniotti, P. Gruber, S. Fallah, W. De Nijs, Torque Distribution Strategies for Energy-Efficient Electric Vehicles With Multiple Drivetrains, *J. Dyn. Syst. Meas. Control.* 139 (12) (2017) 121004, <http://dx.doi.org/10.1115/1.4037003>.
- [22] X. Yuan, J. Wang, Torque distribution strategy for a front- and rear-wheel-driven electric vehicle, *IEEE Trans. Veh. Technol.* 61 (8) (2012) 3365–3374, <http://dx.doi.org/10.1109/TVT.2012.2213282>.
- [23] C.M. Binbin Sun, J. Li, System power loss optimization of electric vehicle driven by front and rear induction motors, *Int. J. Automot. Technol.* 19 (2018) 121–134, <http://dx.doi.org/10.1007/s12239-018-0012-5>.
- [24] A. Pennycott, L.D. Novellis, P. Gruber, A. Sorniotti, Sources of power loss during torque-vectoring for fully electric vehicles, *Int. J. Veh. Des.* 67 (2015) 157–177, <http://dx.doi.org/10.1504/IJVD.2015.068142>.
- [25] T. Kobayashi, E. Katsuyama, H. Sugiura, Y. Hattori, E. Ono, M. Yamamoto, Theoretical analysis of tyre slip power dissipation mechanism using brush model, *Veh. Syst. Dyn.* 58 (8) (2020) 1242–1256, <http://dx.doi.org/10.1080/00423114.2019.1612926>.
- [26] B. Jacobson, *Vehicle Dynamics - Compendium for Course MMF062*, Chalmers University of Technology, 2017.
- [27] F. Un-Noor, S. Padmanaban, L. Mihet-Popa, M.N. Mollah, E. Hossain, A comprehensive study of key electric vehicle (EV) components, technologies, challenges, impacts, and future direction of development, *Energies* 10 (8) (2017) <http://dx.doi.org/10.3390/en10081217>, URL <https://www.mdpi.com/1996-1073/10/8/1217>.
- [28] S. Janardhanan, *On Power Loss Minimisation for Heavy Vehicles with Axle-Wise and Modular Electrical Propulsion and Friction Braking* (Ph.D. thesis), Chalmers University of Technology, Göteborg, Sweden, 2023.
- [29] G. Pellegrino, A. Vagati, B. Boazzo, P. Guglielmi, Comparison of induction and PM synchronous motor drives for EV application including design examples, *IEEE Trans. Ind. Appl.* 48 (6) (2012) 2322–2332, <http://dx.doi.org/10.1109/TIA.2012.2227092>.
- [30] F. N., Handling analysis and control development of commercial trucks with volvo transport models, 2024, [Online]. Available: <https://se.mathworks.com/videos/handling-analysis-and-control-development-of-commercial-trucks-with-volvo-transport-models-1622035211192.html>. (Accessed 05 October 2024).
- [31] L. Laine, J. Andreasson, Control allocation based electronic stability control system for a conventional road vehicle, in: 2007 IEEE Intelligent Transportation Systems Conference, 2007, pp. 514–521, <http://dx.doi.org/10.1109/ITSC.2007.4357632>.
- [32] L. Laine, *Reconfigurable Motion Control Systems For Over-Actuated Road Vehicles* (Ph.D. thesis), Chalmers University of Technology, 2007, <http://dx.doi.org/10.13140/RG.2.2.23751.32166>.
- [33] J. Persson, J. Åkesson, On Torque Vectoring to Improve Steering Predictability While Minimising Power Loss in Heavy Electric Vehicles Using Model Predictive Control (Master's thesis), Chalmers University of Technology, 2022.
- [34] M. Majdandzic, P. Sousthanamath, *Virtual Vehicle Modeling Architecture with Centralized Control* (Master's thesis), Chalmers University of Technology, 2018.
- [35] R.S. Rice, *Measuring Car-Driver Interaction with the GG Diagram*, Tech. Rep., SAE Technical Paper, 1973.
- [36] S. Abuasaker, *Anti-Jerk Controller with Optimisation-Based Self-Tuning* (Ph.D. thesis), University of Surrey, 2016.
- [37] International Organization for Standardization, *Mechanical vibration and shock - Evaluation of human exposure to whole-body vibration - Part 1: General requirements*, 1997, ISO 2631-1:1997, Available from: ISO website.